Ferromagnetic levitation and harmonic trapping of a milligram-scale yttrium iron garnet sphere

Maria Fuwa [,1,*] Ryosuke Sakagami [,2] and Tsuyoshi Tamegai [2]

[1]*Faculty of Science, Gakushuin University, Mejiro-ku, Tokyo 171-8588, Japan*

[2]*Department of Applied Physics, Graduate School of Engineering, The University of Tokyo, Bunkyo-ku, Tokyo 113-8656, Japan*

We report passive magnetic levitation and three-dimensional harmonic trapping of a 0.3-milligram, 0.5-millimeter-diameter yttrium iron garnet sphere at 4 K. The gradient of an external magnetic field is used for vertical trapping, while the finite-size effect of the diamagnetic effect is used for horizontal trapping. The dynamics of the levitated sphere was optically measured to have trapping frequencies of up to around 600 Hz and mechanical Q factors of the order of $Q \sim 10^3$. These results were quantitatively reproduced by three-dimensional finite-element method simulations. Our results can provide a system where magnetism, rigid body motions, microwaves, and optics interact.

I. INTRODUCTION

Levitation of particles in free space provides an experimental platform where external rigid body motion and internal degrees of freedom can freely interact with each other in conditions of extreme environmental isolation. The manipulation and measurement of these dynamics with high precision can open the way to a wide variety of fundamental and applied research [1–6]. Towards this end, various objects ranging from dielectric nanoparticles [7], nanodiamonds [8–10], metals [11], hard magnets [12,13], and diamagnets [14–17] to superconductors [18–20] have been levitated.

Another promising levitation candidate is single-crystal yttrium iron garnet (YIG) for its large volumetric density of spins of $\sim 10^{22}$ μ_B cm^{-3} with a long coherence time of ~ 1 μs [21]. The quanta of collective spin excitations, or magnons, in YIG crystals have been coherently coupled with both microwaves and optical photons through light-matter interactions [22–25]. Utilization of technologies in the field of cavity quantum electrodynamics to enhance interactions [26] has enabled cavity-mediated strong magnon-microwave couplings [27–30], spin current generation [31], and superconducting-qubit-magnon coupling [32] that can resolve single magnons [33] or enable the superposition of magnons [34]. Applications of this growing field range from microwave-to-optical transducers [35–38], non-Hermitian physics [39], nonlinear magnonics [40], magnon lasers [41], and dark-matter searches [42,43] to multimode quantum memories [44].

The combination of these magnonic effects with levitation can provide a system where magnetism, rigid body motions, microwaves, and optics are intertwined. First, the collective enhancement in magnon-microwave coupling can compensate for the decrease in coupling of particle position and a control microwave field with increasing mass. This allows intensive coupling, with coupling strength that is nearly independent of the size and mass of the particle, which allows center-of-mass cooling of a levitated subcentimeter-size particle [45]. Second, the great reduction in clamping losses by levitation may increase magnetostrictive coupling that can allow ground-state cooling of translational motion [46,47]. Third, due to the conservation of angular momentum, a change in spin excitation can lead to its mechanical rotation via the Einstein–de Haas effect [48,49] and its reciprocal Barnett effect [50]. This spin-mechanical coupling may enable the transduction of angular momentum in the quantum regime [51,52], which serves as ultrasensitive torque sensors [53] or magnetometers [54,55].

Here we report the experimental demonstration of a magnetically levitated YIG sphere in cryogenic conditions. The center-of-mass motion is three-dimensional harmonically trapped by utilizing the magnetic field gradient of an external magnetic field for vertical trapping, and the finite-size effect of the diamagnetic effect from a superconductor whose size is close to the YIG sphere for horizontal trapping [56]. Since there is no eddy current damping in a superconductor, our system is a ultimately very low dissipation system. We optically read out the motion of the levitated YIG sphere to determine the trap frequency and motional Q factor. Finally, the experimental results are compared with three-dimensional finite-element method simulations.

II. EXPERIMENTAL SETUP

Our experimental setup is shown in Fig. 1. A commercial YIG sphere of 0.3 mg mass, $d = 0.5$ mm diameter is trapped in a three-dimensional harmonic potential at the center of the hole of a superconductor bulk of inner diameter $d_{sc} = 0.76$ mm and height $h_{sc} = 1.04$ mm, with a slit of angle $\theta_{sc} \sim 40°$. The YIG sphere diameter of $d = 0.5$ mm was chosen for having the longest spin coherence time [28]. A variable external magnetic field is applied to magnetize the yttrium iron garnet (YIG) sphere using a self-made niobium and titanium alloy (NbTi) superconducting solenoid coil with magnet constant 125 mT/A and charging time constant 5×10^{-5} s.

*maria.fuwa.uni@gmail.com
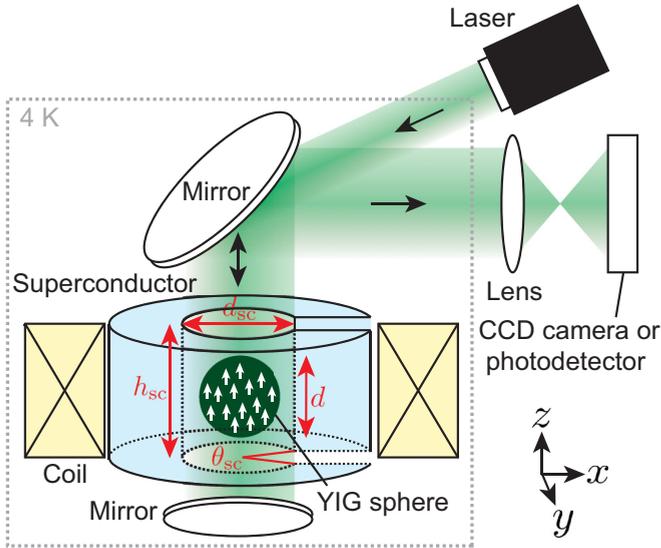
FIG. 1. Schematic overview of experiment.

To increase the magnet constant, this solenoid coil is designed so that the superconductor bulk barely fits into its bore.

Since the superconductor bulk in the diamagnetic state focuses this external magnetic field in the vertical direction (z direction), the YIG sphere is trapped in the center of the superconductor hole where the magnetic flux density is maximum. The magnetic force and trap frequency are

$$F_z = MV \frac{dB_z}{dz}, \qquad (1)$$

$$f_z = \frac{1}{2\pi} \sqrt{\frac{M}{\rho} \frac{d^2 B_z}{dz^2}} \propto \frac{B_z}{d}, \qquad (2)$$

where M is the magnetization, V is the volume, ρ is the density of the YIG sphere, and B_z is the z component of magnetic flux density.

Horizontal (x, y direction) stability is achieved by the finite-size effect of the diamagnetic effect that arises when dimensions of the hole of the superconductor bulk are comparable to the size of the YIG sphere. In this case, the magnetic force on the YIG sphere and resulting trap frequency can only be calculated numerically by integrating the Maxwell stress tensor over its surface. Since the superconductor bulk is zero-field cooled, a slit is introduced to allow the magnetic flux to enter into the hole. The slit shifts the trapping center by a negligible 20 μm closer to the slit from the center of the hole.

We compare our levitation scheme with two kinds of superconductors. One is a cubic melt processed yttrium barium copper oxide (YBCO) with the c axis, the direction perpendicular to the planes of copper-oxide layers, aligned with the direction of the external magnetic field (z direction in Fig. 1). This has a critical temperature $T_c \sim 93$ K [57] and magnetic field tolerance $H_{pen}(0\,\mathrm{K}) \sim 1.2$ T (see Appendix B). Here, H_{pen} is the maximum magnetic field that our superconductor sample could expel by perfect cancellation of their magnetic moments, which depends not only on the type of superconductor, purity, and structural properties, but also highly depends on the shape. Since both the transition temperature and crit-

ical magnetic fields are high, YBCO is expected to retain its superconductivity for higher magnetic fields, enabling higher trapping frequency limits up to 1 kHz for a sphere of the same size, and over 10 kHz for spheres below 100 μm in diameter [56]. This would facilitate ground-state cooling of the center-of-mass motion of micro-gram-scale levitated YIG spheres in the future.

The other is a high-purity single-grain niobium (Nb) with a residual-resistance ratio (RRR) = 582, $T_c \sim 9.3$ K, and $H_{pen}(0\,\mathrm{K}) \sim 125$ mT (see Appendix B). The high RRR indicates that the superconductor is relatively pure with fewer impurities that can disrupt the flow of electrical current through the material. This leads to better superconducting properties and less dissipation from residual resistance, which can lead to eddy current damping. Furthermore, it is more machinable compared to high-temperature superconductors, which can lead to increased design flexibility, improved surface finish, and lower manufacturing costs with faster production times.

III. EXPERIMENTAL RESULTS

The trapping system is cooled to 4 K using a pulse-tube cryocooler (PT407, Cryomech, Inc.). This cryostat is pumped to a pressure of $P = 2 \times 10^{-4}$ Pa with a rotary vane pump and turbo pump. Then, a 5 mW laser at 532 nm (Verdi, Coherent, Inc.) is injected into the cryostat from a window to illuminate the YIG sphere and superconductor. Some of the light is reflected to pass through a telescope with a long focus length of $f = 250$ mm to measure the movement of the YIG sphere using either a CCD camera (DCC1645C-HQ, Thorlabs, Inc.) or photodetector (PDA36A-ED, Thorlabs, Inc.). To reduce seismic noise, the cryostat was vacuum sealed and both the cryocooler and vacuum pumps were turned off during data acquisition.

Initially, the YIG sphere is placed at the bottom of the superconductor hole. Then it is lifted up by applying an external magnetic field above $B_z \geqslant 7.5$ mT. This excites a vertical oscillation, as the YIG sphere is trapped at the center of the hole (Fig. 2) [58]. To measure the oscillations, a photodetector is placed at the end of the telescope to monitor the change in optical intensity as the YIG sphere moves. 1 250 000 points were acquired using a data logger (DLM2025, Yokogawa Electric Corporation) at a sampling frequency of 125 kHz for a measurement time of 10 seconds. The base plate temperature was monitored during this measurement, which started at 3.8 K and increased to a maximum of 4.6 K.

Modes have been identified by comparing the trapping frequencies to the frequencies predicted for this configuration by a three-dimensional finite-element analysis using COMSOL MULTIPHYSICS (see Appendix C). Since the easy axis of the levitated sphere is aligned with B_z, it is rotationally symmetric and only the translation oscillations are detected. Figure 3(a) shows the dependence of the trapping frequency on the external magnetic field density $B_z = 12.5 - 75$ mT for superconductors YBCO and Nb. Since B_z is below the saturation magnetization of YIG at $M_s = 196$ kA/m, the trapping frequencies should linearly increase with B_z as

$$f_z\,[\mathrm{Hz}] = 5.6 \times 10^{-3} B_z\,[\mathrm{T}], \qquad (3)$$

$$f_y \sim 1.6 f_z, \qquad f_x \sim 1.5 f_z. \qquad (4)$$
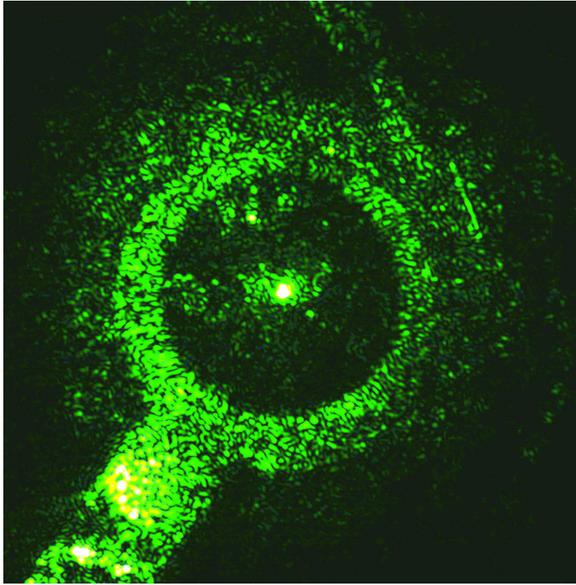
FIG. 2. Photograph of a levitated $d = 0.5$ mm YIG sphere trapped in the center of the YBCO hole observed using a CCD camera.

This is variable in the range of 50 Hz to as high as 600 Hz. The maximum trapping frequency is limited by the maximum current of 0.6 A that can be applied to our homemade superconducting coil due to joule heating.

For YBCO, the vertical trapping frequencies match the simulated prediction. Since the initial position of the YIG sphere is slightly shifted from the center of the superconductor hole, diagonal oscillations are also excited during the lift-off process. These diagonal oscillations have frequencies in the range $f_z \leqslant f_r \leqslant f_y$, which match the theoretical prediction.

In the case of Nb, both the vertical and diagonal trapping frequencies are close to the simulated prediction. However, the discrepancy increases with the external magnetic field. This is likely due to the fact that the system temperature of 4 K is close to the critical temperature T_c of Nb, and restoring force from the diamagnetic effect weakens as the persistent current approaches the critical current J_c. Thus, it is likely that Nb has an effective inner diameter that is larger than the actual diameter d_{sc}, leading to a slightly weaker trapping potential and lower trapping frequency.

A typical frequency spectrum of the levitating YIG sphere shows how the magnetic trapping gets stronger with increasing B_z [Fig. 3(b)]. The amplitude of the oscillations have been calibrated from the maximum oscillation amplitude being the lift distance of 0.25 mm. For $B_z = 12.5$ mT, the magnetic spring is weak and multiple peaks are observed near the expected trapping frequency, indicating a fluctuation in YIG sphere position. Since the vertical and horizontal trapping frequencies are close, it is difficult to resolve these modes. As the external magnetic field increases to $B_z \geqslant 37.5$ mT, distinct vertical and diagonal oscillations can be observed, indicating that only the desired modes are excited.

The Q factor is measured by exciting oscillations by lifting up the YIG sphere and observing the amplitude decay of the envelope. The frequency modes were isolated with the use of
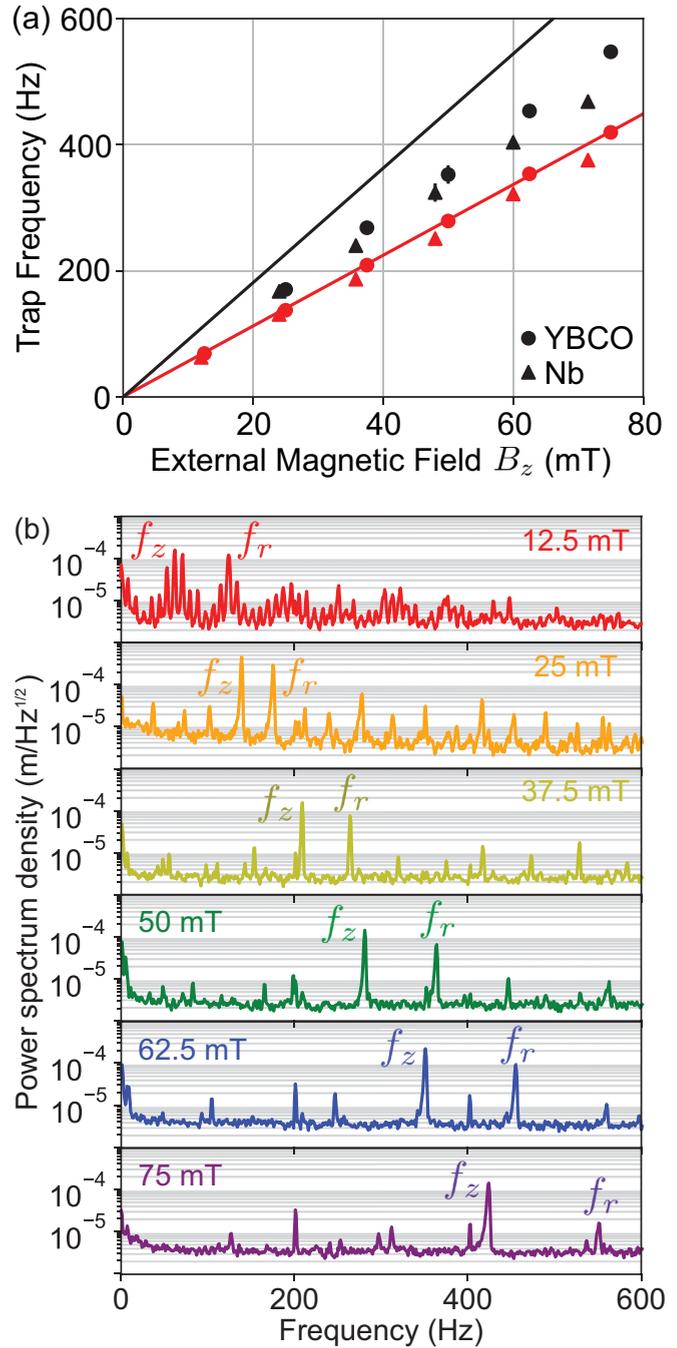
FIG. 3. (a) Trap frequency for varying external magnetic fields B_z. Red: vertical oscillation f_z (z direction in Fig. 1); black: horizontal oscillation f_y (y direction in Fig. 1); solid line: simulated trap frequencies, plotted with experimentally observed frequencies for YBCO (circle) and Nb (triangle) as superconductor, respectively. (b) Power spectrum density for varying external magnetic fields B_z. f_z: vertical oscillations; f_r: diagonal oscillations.

a band-pass filter, and the decay is fitted to an exponential function of time constant τ, with a relative fitting error below $<10^{-3}$. Finally, the Q factor is calculated as $Q = 2\pi f_i/\tau$, where f_i is the trap frequency obtained by Fourier transforming the decaying oscillations. The resolution of the trapping frequency f_i is limited to 0.1 Hz due to the measurement time of 10 s.
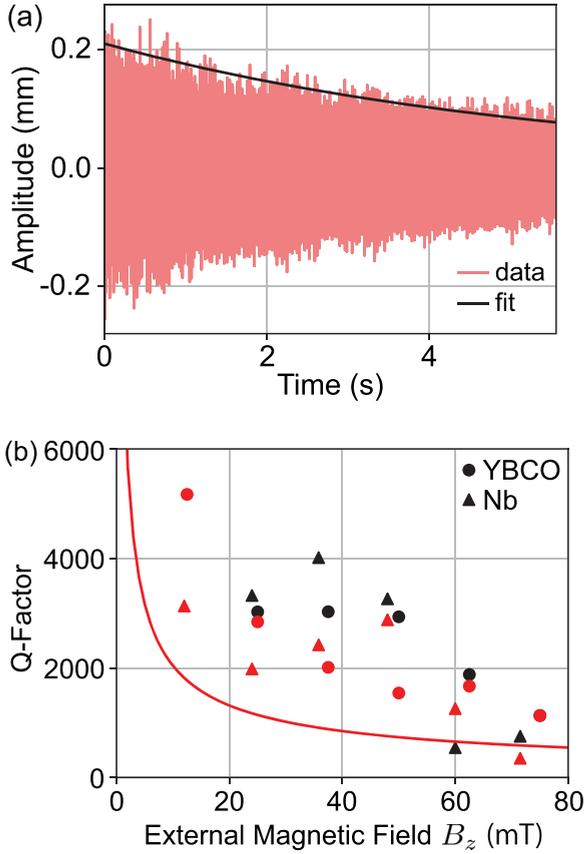
FIG. 4. (a) Example of measured amplitude decay for $B_z = 25$ mT, $f_r = 169$ Hz. (b) Mechanical Q factors for varying external magnetic fields B_z. Circle: YBCO as superconductor; triangle: Nb as superconductor; red: vertical oscillations at frequency f_z; black: diagonal oscillations at frequency f_r in Fig. 3. Red line: theoretically predicted Q factor for the vertical oscillation mode (z direction in Fig. 1) at frequency f_z.

All modes had Q factors of the order of 10^3, which decreased with increasing B_z (Fig. 4). No significant Q-factor difference was observed between YBCO and Nb as superconductor. The Q-factor limit from eddy current damping was predicted by a three-dimensional finite-element analysis using COMSOL MULTIPHYSICS (see Appendix C), assuming the electrical conductivity $\sigma = 6.58 \times 10^9$ S/m for pure oxygen-free copper at 10 K [59]. This scales as $Q_{\mathrm{eddy}, z} \propto B^{-0.5}$ and is inversely proportional to the electric conductivity $Q_{\mathrm{eddy}, z} \propto \sigma^{-1}$. The experimentally measured Q factors agreed in order with simulated predictions and obeyed the same tendency of decreasing with external magnetic field. The discrepancy is likely due to the actual electrical conductivity of oxygen-free copper being lower than σ, due to material variability or local heating by the coil currents and injected light, and the Q factor limited by the eddy current damping could be higher. These results suggest that eddy currents are likely to be the dominant loss in our system. Experimental optimization of external magnetic field B_z will be conducted elsewhere.

The Q factors for horizontal oscillations (x, y directions in Fig. 1) were expected to have an order higher Q factor compared to vertical oscillations (z direction in Fig. 1). This

is likely because vertical oscillations induce eddy currents that circulate in a helical pattern around the cylinder's axis, which creates a secondary magnetic field aligned with the YIG magnetization and therefore leads to significant damping. On the other hand, horizontal oscillations induce currents around the circumference of the cylinder in a direction perpendicular to its axis, which can create a secondary magnetic field perpendicular with the YIG magnetization and therefore lead to less damping. Since the diagonal oscillations are a combination of vertical and horizontal oscillations, they have higher Q factors than vertical oscillations.

These eddy current dampings can be significantly reduced to $Q_{\mathrm{eddy}, z} > 10^8$ by either increasing the bore diameter of the superconducting coil to over 40 mm, using a Helmholtz coil configuration, or adding slits to the bobbin to mitigate eddy current flow, and positioning any metal planer stages over 10 mm away. In addition, the utilization of dielectric material such as fused silica or sapphire for jigs instead of oxygen-free copper is expected to significantly reduce the eddy current damping. Meanwhile, the gas damping limited Q factor is expected to be over $Q_{\mathrm{gas}} > 10^{11}$ for our system. Thus, our system has the potential to reach eddy current limited Q factors that are over 10^8 for spheres below 0.2 mm in diameter [56].

This high Q factor, together with intensive spin-mechanical coupling, can enable phononic and magnonic ground-state cooled YIG spheres below 0.15 mm in diameter with a trapping frequency above $f_z > 10$ kHz, under an external magnetic field of $B_z = 1.2$ T, ferromagnetic resonance of 30 GHz, and linewidth below 0.3 MHz at 10 mK [45,56]. Applications range from magnonic quantum networks [60] and quantum tunneling [61] to the generation of spatial superpositions [62]. Furthermore, since a levitated YIG sphere can be an isolated quantum system which conserves the angular momentum, it may allow coherent superpositions of quantized rotational states through spin-mechanical interactions or gyromagnetic effects, which enable highly sensitive gyroscopes [63]. These rotational states may be read out using optical birefringence or by attaching metasurface polarizers [64] for polarization extinction measurements.

IV. CONCLUSION

In conclusion, a YIG sphere of 0.3 mg mass and 0.5 mm diameter is levitated and three-dimensional harmonically trapped in the center of a superconductor hole with slit. The trap frequency increased linearly with the external magnetic field strength and was variable from 50 Hz up to 600 Hz. The Q factor for translational oscillations was limited to the order of $Q \sim 10^3$ due to eddy current damping. A three-dimensional finite-element method is used to explain the levitation dynamics and main source of dissipation of the particles' motion, which qualitatively reproduced the experimental results. This research lays the foundation for future research and development of levitated YIG systems that can interact with microwaves, superconducting qubits, acoustic phonons, or optical photons.

APPENDIX A: EXPERIMENTAL SETUP DETAILS

The YIG sphere is a pure single crystal grown using the floating zone method, diced and polished into spheres by Microsphere, Inc. The YBCO is cubic melt processed, commercially made by Nippon Steel Corporation, and machined into a Landolt ring shape, with the c axis, the direction perpendicular to the planes of copper-oxide layers, aligned with the axis of the cylindrical hole. The high-RRR niobium (Nb) ingot is custom grown using electron beam melting by ULVAC, Inc. and machined into a Landolt ring shape by KEK Mechanical Engineering Center.

The niobium and titanium alloy (NbTi) superconducting solenoid coil has a winding inner diameter of 3.1 mm, outer diameter of 13 mm, height of 1 mm, total number of turns of 475, using a wire of diameter 0.1 mm, inductance 1.3 mH, and charging time constant 5×10^{-5} s. It is designed with a bore diameter $d_{\text{bore}} = 2.274$ mm that is slightly larger than the superconductor bulk to enlarge the magnet constant of 125 mT/A. The YIG sphere is enclosed inside the superconductor hole by attaching a piece of microscope cover glass of thickness $\sim$0.17 mm on the top and bottom of the superconductor bulk hole as lids with varnish (GE7031). This superconductor piece is then glued onto the superconductor coil bore with varnish to ensure enough heat conduction. Thus the initial YIG position is at the bottom of the superconductor bulk hole, and is lifted up and trapped in the center when an external magnetic field is applied. This structure is placed beneath a half-inch mirror and positioned on a 4 K stage (Fig. 5). Note that at the center of the superconductor hole, the external magnetic field B_z is focused in the vertical direction and is minimum in the horizontal direction. If the superconductor does not exhibit diamagnetism, the YIG sphere will stick to the side of the superconductor hole where the horizontal magnetic field is maximum, and therefore no oscillations will be observed. A summary of the experimental parameters is given in Table I.

1. Optical heating

Visible light shown onto the YIG sphere for illumination can lead to a local temperature increase of the levitated YIG sphere. Here a lens of focus length $f = 750$ mm is used to focus the optical beam to a diameter of $d_{\text{opt}} \sim 0.9$ mm at the
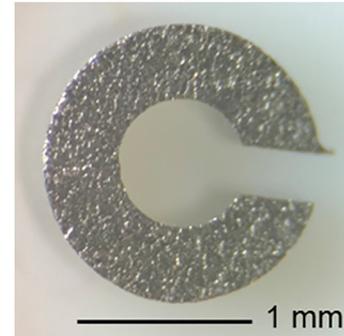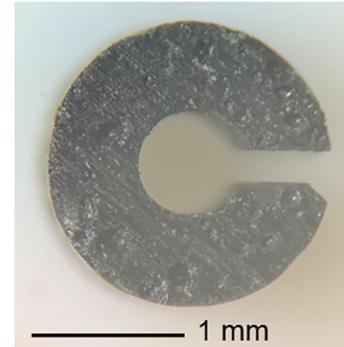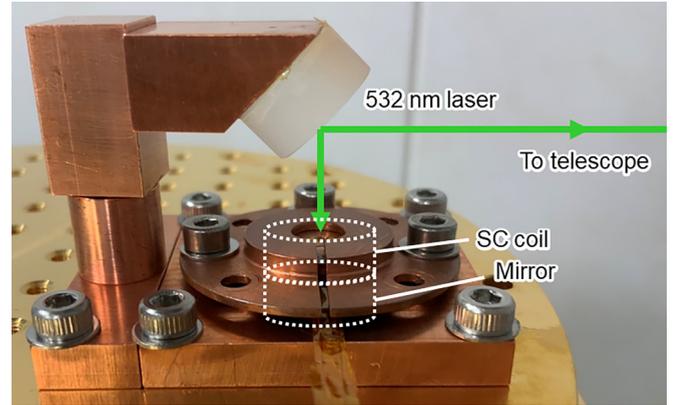
FIG. 5. Top: Photograph of experimental setup; middle: YBCO sample; bottom: niobium sample.

YIG sphere. Out of this, the $P_{\text{opt}} = 5$ mW input beam,

$$\frac{P_{\text{opt}}}{\sqrt{2\pi}\, d_{\text{opt}}/2} \int_{-d/2}^{d/2} \exp\left(-\frac{x^2}{d_{\text{opt}}}\right) dx \sim 2.8 \text{ mW}, \qquad \text{(A1)}$$

hits the $d = 0.5$ mm diameter YIG sphere. For a 532 nm laser, with reflectivity of $R_{532\,\text{nm}} \sim 0.17$ [67] for a polished bulk YIG, and absorption coefficient $\alpha = 10^3 \,\text{cm}^{-1}$ [68], $\dot{q}_{\text{opt}} = 2.35$ mW of the illuminated light is absorbed. During the measurement time of 10 s, the YIG sphere is optically heated by $\Delta E_{\text{opt}} = 23.5$ mJ.

Since the cooling power of our cryostat of 0.5 W for the superconductor bulk and YIG sphere is much larger than $\dot{q}_{\text{opt}}$, we assume that only the temperature of the levitated YIG sphere increases to T_2, and everything nearby remains at $T_1 = 4$ K. Bulk YIG has a thermal conductivity of $\kappa_{\text{YIG}}(4\,\text{K}) = 10.5$ W/m K and specific heat of $C_v(4\,\text{K}) = 0.02$ J/kg K, both of which increase with temperature [69]. The thermal conductiv-

TABLE I. Summary of experimental parameters.

Quantity	Symbol	Value	Unit
YIG sphere diameter	d	0.5	mm
YBCO bulk hole inner diameter	d_{sc}	0.756	mm
YBCO bulk outer diameter	$d_{\text{sc out}}$	1.948	mm
YBCO bulk height	h_{sc}	1.039	mm
YBCO bulk slit angle	θ_{sc}	39	deg
Nb bulk hole inner diameter	d_{sc}	0.758	mm
Nb bulk outer diameter	$d_{\text{sc out}}$	1.684	mm
Nb bulk height	h_{sc}	1.029	mm
Nb bulk slit angle	θ_{sc}	42	deg
Superconductor coil wire diameter	d_{coil}	102	μm
Superconductor coil number of turns	N_{coil}	475	
Superconductor coil height	h_{mag}	1	mm
Bobbin bore diameter	d_{bore}	2.274	mm
Bobbin thickness		0.5	mm
Bobbin outer diameter		14	mm
Bobbin height		2	mm
Copper lid inner diameter		6	mm
Copper lid outer diameter		14	mm
Copper lid thickness		1	mm
YIG density		5172	kg/m^3
YIG sphere mass	m	0.339	mg
YIG relative permeability [65]	μ_γ	32	
YIG relative permittivity [66]	ε_γ	15	
Conductivity of oxygen-free copper	σ_{Cu}	6.58×10^9	S/m
Conductivity of insulators		1	S/m
Air and copper relative permeability		1	

ity throughout the YIG sphere is approximately

$$\kappa_{\text{YIG}} \times \pi \left(\frac{d}{2}\right)^2 \times \frac{1}{d} \times (T_2 - T_1). \tag{A2}$$

This gives 8.27 mW for $T_2 = 5$ K, which is larger than $\dot{q}_{\text{opt}}$. Thus we can assume the temperature is uniform over the sphere.

The heat capacity of the YIG sphere can be modeled using the Debye model as

$$C_v(T) \propto \left(\frac{T}{T_D}\right)^3 \int_0^{\frac{T_D}{T}} \frac{x^4 e^x}{(e^x - 1)^2} \, dx, \tag{A3}$$

with Debye temperature $T_D = 531$ K and proportional coefficient 2085 J/kg K [69]. The optical heating can increase the YIG sphere temperature up to $T_2 \sim 246$ K, which satisfies

$$\Delta E_{\text{opt}} \sim m \int_{T_1}^{T_2} C_v(\tau) \, d\tau = 23.7 \text{ mJ}, \tag{A4}$$

with $C_v(246 \text{ K}) = 556.6$ J/kg K. This is due to the large absorption of visible light by YIG, as well as the small mass $m = 0.339$ mg of the YIG sphere.

In this case, the radiative heat transfer from the levitated sphere to the glass plates on the top and bottom of the superconductor bulk hole is negligible,

$$\dot{q}_{\text{rad}} = \sigma_{\text{SB}} E A_{\text{YIG}} (T_2^4 - T_1^4) \sim 8.6 \text{ μW}. \tag{A5}$$

Here, $\sigma_{\text{SB}} = 5.67 \times 10^{-8}$ W/m^2 K^4 is the Stefan-Boltzman constant,

$$E = \frac{\varepsilon_1 \varepsilon_2}{\varepsilon_2 + A_{\text{YIG}}/A_{\text{env}}(\varepsilon_1 - \varepsilon_1 \varepsilon_2)},$$

with emittivity $\varepsilon_1 = \varepsilon_2 = 0.9$ for nonmetallic surfaces, $A_{\text{YIG}} = 7.85 \times 10^{-7}$ m^2 the surface area of the YIG sphere, and $A_{\text{env}} = 1.3 \times 10^{-4}$ m^2 the surface area of the two glass plates [59]. Since the emittivity scales as the square root of a material's resistivity for metals, there is no heat transfer to the superconductor bulk, which reflects all radiative heat.

The heat conduction through gas in the free molecular regime is negligible,

$$\dot{q}_{\text{gas}} = 1.2 \times \frac{0.5}{1 + 0.5 A_{\text{env}}/A_{\text{YIG}}} P A_{\text{YIG}} (T_2 - T_1) \sim 0.45 \text{ μW}, \tag{A6}$$

for $P = 2 \times 10^{-3}$ Pa [59].

Thus, it is possible that the temperature of the levitated YIG increased to as high as $T_2 \sim 246$ K. During the experiment, the YIG sphere was repetitively cooled back down to $T_2 = T_1 = 4$ K in between measurements, when the YIG sphere is lowered back to its initial position at the bottom of the superconductor hole on top of a glass plate. For quantum technology applications, optical heating can be circumvented by attaching a metasurface mirror to the YIG sphere or by using an infrared laser near 1.55 μm, where YIG is transparent.

APPENDIX B: SUPERCONDUCTOR PROPERTIES

Although the superconducting properties of bulk YBCO and Nb are well known, the properties of the actual material used, i.e., the effect of shape and damage applied through machining, are unknown. To asses this, we measured the superconducting properties of samples machined from the same bulk to estimate the properties of the samples in Fig. 5.

1. Critical temperature T_c measurement

The superconductor critical temperature T_c can be determined by measuring the magnetic moment of the superconductor as a function of temperature, while the material is subjected to a low external magnetic field of 0.5 mT (5 Oe). Below T_c, the superconductor will expel the magnetic field due to the diamagnetic shielding effect, leading to a drop in the magnetic moment. The magnetic moment was measured using a superconducting quantum interference device (SQUID) magnetometer (MPMS-XL5, Quantum Design, Inc.). The critical temperature is determined as the temperature at which the magnetic moment begins to decrease rapidly.

We measured the critical temperature for the custom-made high-RRR Nb sample, which had a transition temperature of $T_c \sim 9.3$ K (Fig. 6). This agrees with the bulk value of $T_c = 9.26$ K for Nb [70]. The sharp drop in the magnetic moment of Nb reflects its purity and good superconducting properties. Note that since the YBCO ring is made from a commercial bulk, and its transition temperature of $T_c = 93$ K [57] is well above our levitation conditions at 4 K, indicating that it can be assumed to be in a superconducting state albeit
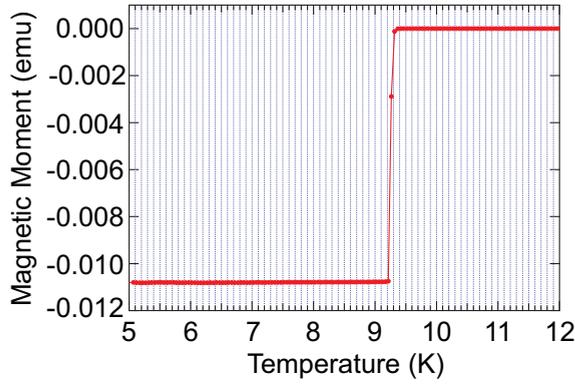
FIG. 6. Magnetic moment temperature dependence for Nb.

with temperature fluctuations, the transition temperature of a machined sample has not been measured.

2. Critical current density $J_c(T, B)$ estimation

The critical current density J_c of a superconductor is the maximum electrical current density that can flow through it without causing energy dissipation due to vortex motion. The temperature and external magnetic-field-dependent critical current density can be calculated from the magnetic moment using the Bean model [71,72]. This is a phenomenological model that assumes a spatially uniform critical current density independent of the applied magnetic field. Here the current density $j = J_c$ inside the superconductor follows the Ampére's law,

$$\frac{dB_z}{dx} = \mu_0 j, \tag{B1}$$

where z is the direction of the magnetic field B. The image field created inside the superconductor by this current is

$$B_z(x) = \mu_0 J_c x + \text{const}, \tag{B2}$$

which decreases linearly with the distance from the superconductor surface.

The *M-H* curve of the Nb sample used for the J_c measurement is given in Fig. 7(a). The fluctuations in the magnetic moment at 2 and 3 K are due to flux jumps caused by magnetic flux avalanches, i.e., the rapid invasion of a large number of quantized magnetic flux due to thermomagnetic instability. The negative value of the magnetic moment in the field-decreasing branch indicates that the irreversible magnetic moment is smaller than the reversible one due to weak flux pinning. This Nb sample is a cylinder, which creates a cone-shaped magnetic field profile and the magnetic moment is given by

$$m_{sc} = \frac{1}{2} \int r \times J_c \, dr = J_c \int dr \int dz \, \pi r^2 = \pi J_c \frac{a^3}{3} h_{sc}, \tag{B3}$$

where a and h_{sc} are the radius and height. The superconductor magnetization is

$$M_{sc} = \frac{m_{sc}}{V} = \pi J_c \frac{a^3 h_{sc}}{3} \frac{1}{\pi a^2 h_{sc}} = \frac{J_c a}{3}, \tag{B4}$$
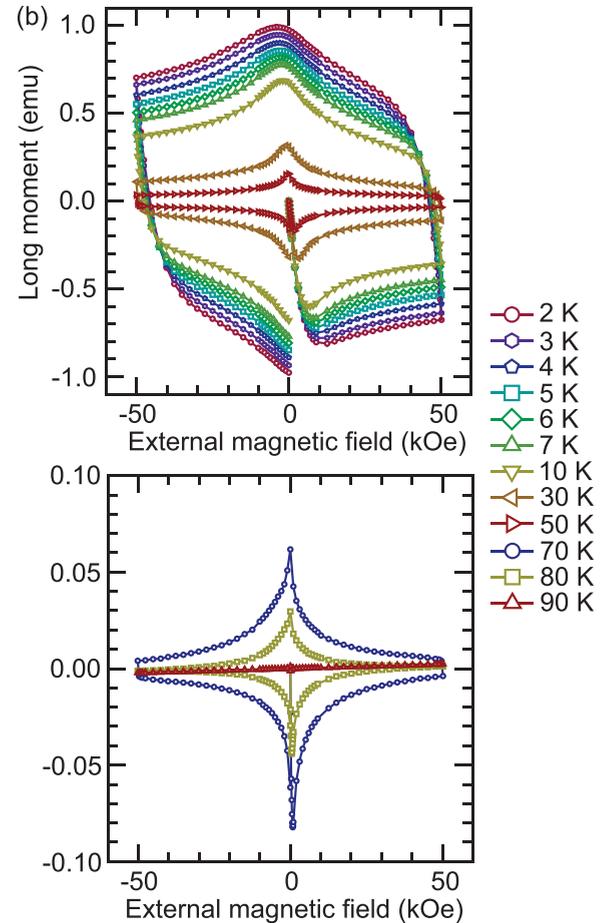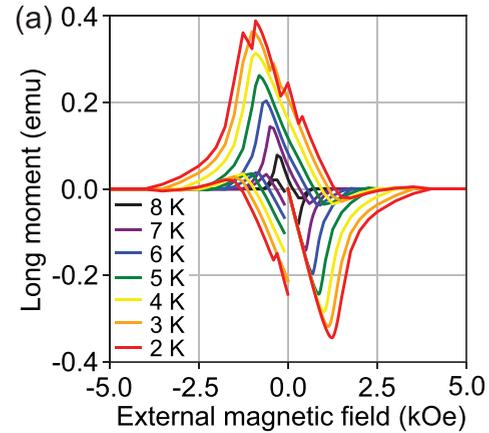
FIG. 7. Magnetic moment dependence on temperature and applied magnetic field for (a) Nb and (b) YBCO.

where V the volume of the cylinder. Solving this for J_c gives

$$J_c = \frac{3M_{sc}}{a}. \tag{B5}$$

This critical current density is called the "magnetic critical current density," which gives the maximum current density that a superconductor can carry before it starts to dissipate energy. From Fig. 7(a), $m_{sc}(4 \text{ K}, 0 \text{ mT}) \sim 0.16 \text{ emu} = 1.6 \times 10^{-4} \text{ A/m}^2$ for a Nb sample of $a = 0.835 \text{ mm}$, $V = 2.28 \times 10^{-9} \text{ m}^3$ gives $M_{sc}(4 \text{ K}, 0 \text{ mT}) \sim 7.0 \times 10^4 \text{ A/m}^2$ and $J_c(4 \text{ K}, 0 \text{ mT}) \sim 2.5 \times 10^8 \text{ A/m}^2$. This is
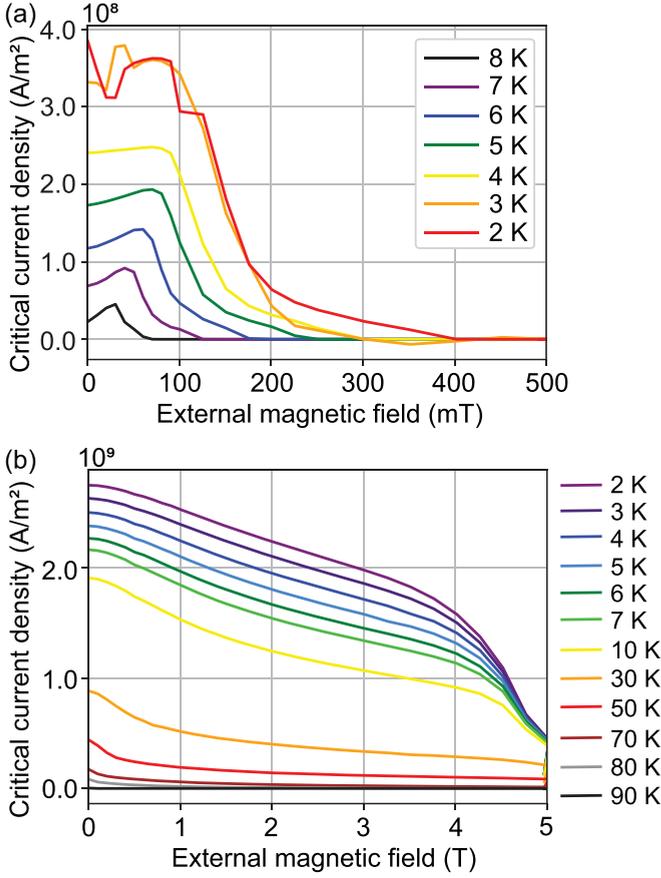
FIG. 8. Temperature and magnetic field dependence of J_c for (a) Nb and (b) YBCO.

much lower than the value measured for Nb thin films at 2.0×10^{10} A/m² at 4.2 K [73]. The temperature and external magnetic field dependence of J_c are given in Fig. 8(a).

The M-H curve for the YBCO sample used for the J_c measurement is given in Fig. 7(b). Due to the strong flux pinning force of YBCO, it retains a large amount of trapped magnetic flux after the external field is removed, and the M-H curve exhibits a large magnetic hysteresis loop. This YBCO sample is a cylindrical structure with a hole and two slits along the radial direction. Thus we model our superconductor as two rectangles with width a, length b $(a < b)$, and height c, of which J_c is given by

$$m'_{sc} = 2 \iint S(x)J_c \, dx dz$$

$$= 2cJ_c \int_0^{\frac{a}{2}} [4x^2 + 2x(b-a)] \, dx$$

$$= \frac{1}{2}J_c a^2 bc \left(1 - \frac{a}{3b}\right), \tag{B6}$$

$$M'_{sc} = \frac{m'_{sc}}{V'} = \frac{1}{2}J_c a^2 bc \left(1 - \frac{a}{3b}\right)\frac{1}{2abc}$$

$$= \frac{1}{4}J_c a \left(1 - \frac{a}{3b}\right), \tag{B7}$$

$$J_c = \frac{4M'_{sc}}{a\left(1 - \frac{a}{3b}\right)}, \tag{B8}$$

with $S(x)$ being the cross-sectional area normal to the external magnetic field, $a = (d_{sc\,out} - d_{sc})/2$, $b = \pi(d_{sc\,out} + d_{sc})/4$. From Fig. 7(b), $m_{sc}(4\,K, 0\,mT) \sim 0.89$ emu $= 8.9 \times 10^{-4}$ A/m² for a YBCO sample of $a = 0.596$ mm, $b = 2.124$ mm, $V' = 2.63 \times 10^{-9}$ m³ gives $M_{sc}(4\,K, 0\,mT) \sim 3.4 \times 10^5$ A/m² and $J_c(4\,K, 0\,mT) \sim 2.5 \times 10^9$ A/m². This is higher than the critical current density of Nb, and much lower than the critical current density measured for YBCO wires at 2.0×10^{11} A/m² at 4.2 K [74]. The temperature and external magnetic field dependence are given in Fig. 8(b). To measure the full phase diagram of J_c, it is necessary to measure the full magnetic moment hysteresis curve using high enough external magnetic fields. Since the external magnetic field of 5 T was not high enough, artifacts are introduced in the form of an abrupt decrease in J_c above 4 T for temperatures below 10 K.

3. Pinning force density $F_p(T, B)$ estimation

When a magnetic field is applied to a type-II superconductor, vortices, which each carry a quantized magnetic flux, can penetrate the material. For low magnetic fields, the superconductor is in the vortex solid state, where vortices in a superconductor form a lattice. In the absence of any external forces, these vortices are pinned by defects and impurities in the material, resulting in a static arrangement. The superconductor is in a mixed state where both superconducting and normal conducting regions coexist within the material. When the temperature or magnetic field exceeds the critical limit, the superconductor transitions into a vortex liquid state. Vortices move freely throughout the superconductor in a disordered manner, due to thermal fluctuations, external magnetic fields, or interactions with each other, exhibiting fluidlike behavior. The motion of vortices causes substantial energy dissipation and this phase is therefore not suitable for levitation.

This critical magnetic field can be estimated by the flux pinning force density $F_p = J_c B$, which is a measure of the maximum pinning force per unit volume that can be exerted on vortices in a superconductor before they start to move (Fig. 9). This flux pinning force increases with applied magnetic field because the magnetic field increases the number of vortices, enhances the interaction between the vortices and the pinning centers, making it more difficult for them to move or escape their pinned positions. However, beyond a certain magnetic field strength H_{fp}, the stronger pinning centers become fully occupied or saturated and additional vortices cannot be effectively pinned, reducing the ability to trap and immobilize vortices. Figure 9(a) shows that magnetic fields above $H_{fp} \sim 100$ mT may cause vortex movement for temperatures below 4 K. This critical magnetic field decreases with increasing temperature. For $B_z \leqslant 75$ mT used for YIG levitation, vortex movement-induced dissipation will arise for $T > 6$ K. Figure 9(b), together with Figs. 7(b) and 8(b), shows that the peak in pinning force density is due to the artifacts in the J_c measurement introduced by insufficient maximum external magnetic field strength. Thus, $H_{fp} > 5$ T and there is no vortex movement for magnetic fields below 5 T.

4. Magnetic field tolerance $H_{pen}(T)$ estimation

We estimate H_{pen}, the maximum magnetic field our superconductor sample could expel by perfect cancellation of
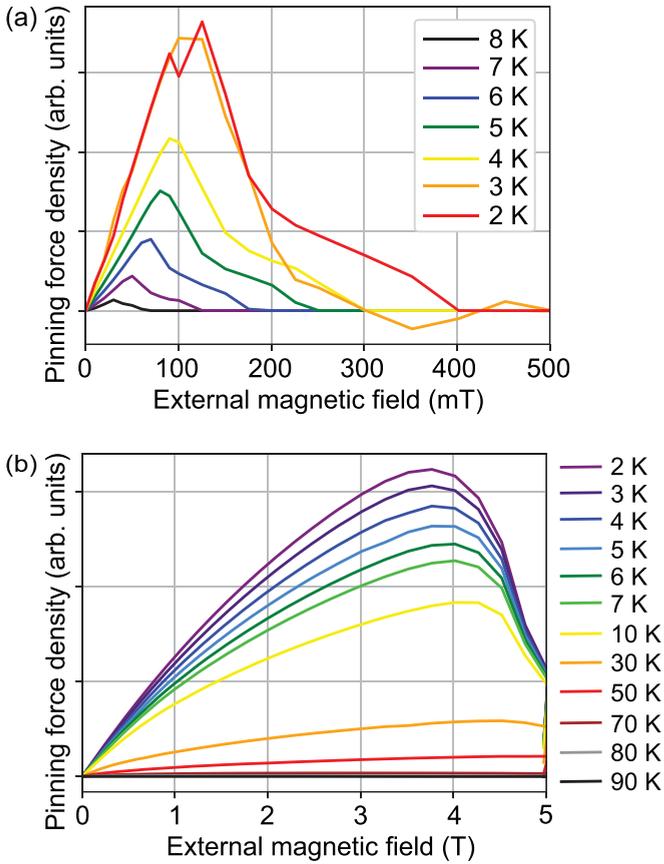
FIG. 9. Temperature and magnetic field dependence of F_p for (a) Nb and (b) YBCO.

their magnetic moments, which depends not only on the type of superconductor, purity, and structural properties, but also the shape. This can be estimated from Fig. 7 as the external magnetic field when the modulus of the magnetic moment of a superconductor is maximum (Fig. 10).

For pure Nb, H_{pen} follows the same temperature-dependence curve as the critical magnetic field H_c, and the experimental data can be fitted to

$$H_{pen}(T) = H_{pen}(0)\left[1 - \left(\frac{T}{T_c}\right)^{\gamma}\right], \quad (B9)$$

with $T_c = 9.26$ K, $\gamma = 2.13$ predicted from the Bardeen-Cooper-Schrieffer (BCS) theory. This shows that the Nb is in a diamagnetic state for magnetic fields below H_{pen}. The maximum magnetic field that our sample can tolerate at 0 K is $H_{pen}(0) = 122 \pm 21$ mT. Assuming the temperature of the Nb bulk is equal to the base plate, for YIG levitation conditions of $T \leqslant 4.6$ K, $H_{pen}(4.6 \text{ K}) \sim 94$ mT is larger than the applied magnetic fields. However, since the external magnetic field B_z is close to H_{pen}, local damage in our Nb sample can lead to flux penetrations and increase effective Nb hole inner diameter d_{sc}, as expected from trap frequency measurements.

The magnetic field tolerance $H_{pen}(4.6 \text{ K}) \sim 900$ mT proves that the YBCO sample expelled magnetic flux completely during the entire experiment [Fig. 10(b)]. The sharp increase of H_{pen} at low temperatures is due to strong flux pinning in YBCO. Further research on how strongly pinned vortices
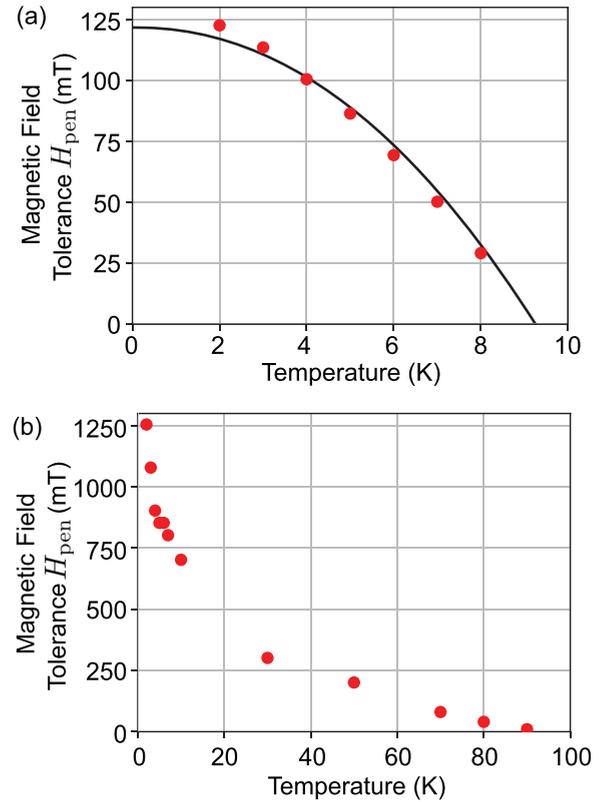
FIG. 10. Temperature dependence of H_{pen} for (a) Nb and (b) YBCO.

affect the eddy current damping at higher external magnetic fields will be conducted elsewhere.

APPENDIX C: THREE-DIMENSIONAL FINITE-ELEMENT METHOD SIMULATIONS

A three-dimensional COMSOL model was constructed using the parameters in Table I to simulate the dynamics of the levitated YIG sphere.

1. Trap potential

First the three-dimensional magnetic field distribution is calculated by a stationary study, using the Ampére's law. Since the external magnetic field that is applied is lower than the saturation magnetization of pure YIG at low temperatures, $M_s = 196$ kA/m ($\mu_0 M_s \sim 246$ mT), we use the relative permeability $\mu_{\gamma} = 32$ [65] to calculate the constitutive relation $B = \mu_0\mu_{\gamma}H$ used during this calculation. This allows the YIG magnetization to both spatially and temporary respond to the changing magnetic field, which is consistent with the fact that it cannot be treated as a single-domain magnetic dipole. The resulting force on the YIG sphere was calculated by numerically integrating the Maxwell stress tensor,

$$\mathbf{F}_{em} = \iint \frac{\mathbf{B}_n \cdot \mathbf{B}_n}{2\mu_0}\, dS, \quad (C1)$$

where $\mathbf{B}_n$ is the normal component of the magnetic flux density.
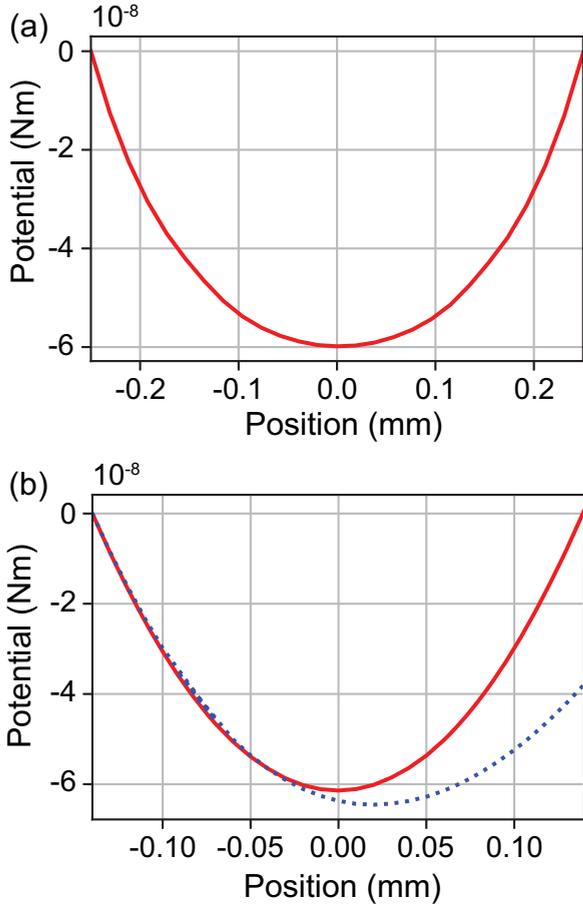
FIG. 11. Trap potential of $d = 0.5$ mm YIG sphere under an external magnetic field of $B_z = 37.5$ mT (a) vertical trapping potential (z direction in Fig. 1), (b) horizontal trapping potential in red solid line: perpendicular to the slit (y direction in Fig. 1), and blue dotted line: in the direction of the slit (x direction in Fig. 1).

In order to accurately calculate the force on the YIG sphere, constructing a fine enough mesh is crucial. We calculated the forces on the YIG sphere with varying maximum and minimum mesh sizes to resolve the small regions between the sphere and superconducting wall. A mesh conversion analysis showed that a minimum mesh size of $d/100 = 5$ μm and largest mesh size of $d/20 = 25$ μm was required to calculate the force on a YIG sphere of $d = 0.5$ mm with an accuracy of over two significant figures. This was used to calculate the force on the YIG sphere as a function of its position. Subsequently, this was numerically integrated to obtain the trapping potential (Fig. 11). This shows that the YIG sphere is indeed trapped in a harmonic potential with its center shifted around 20 μm from the center of the hole towards the slit.

2. Trap frequency

The dynamics of the YIG sphere is simulated by a time-domain study that calculates first-order ordinary differential equations,

$$\dot{v} = F_{\text{em}}/m, \tag{C2}$$

$$\dot{u} = u, \tag{C3}$$
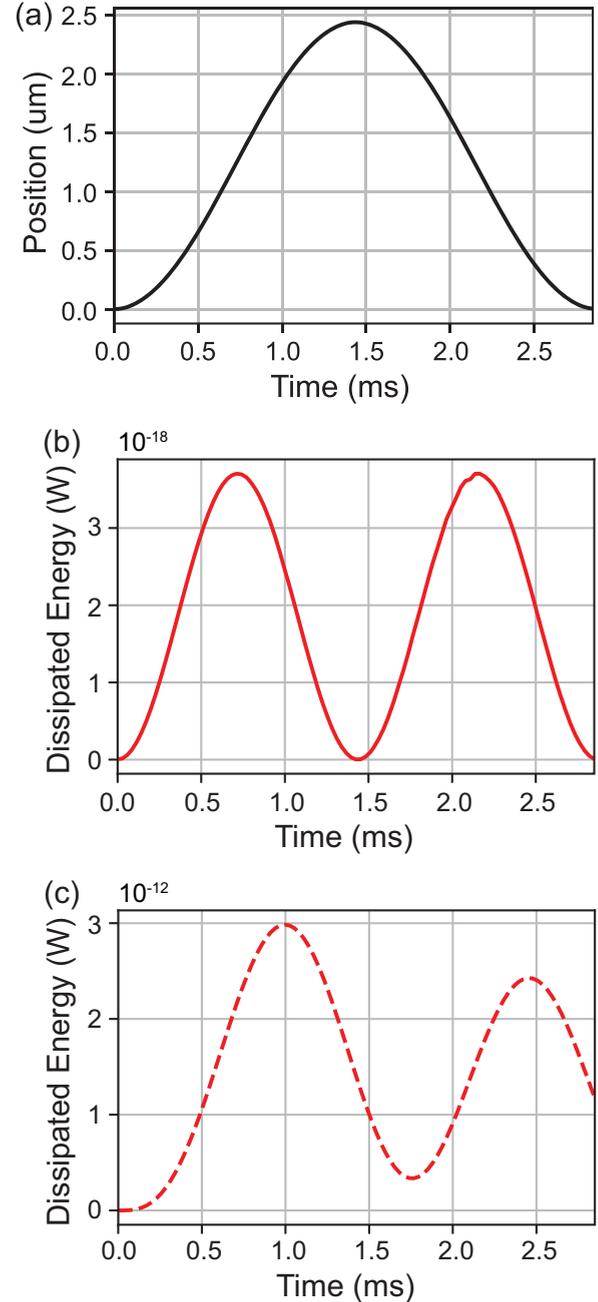
FIG. 12. Example of time-dependent electro-magnetic energy loss during a single oscillation for $B_z = 62.5$ mT. (a) YIG position, (b) energy dissipation in YIG sphere, (c) total energy dissipation in superconductor coil bobbin, base plate, and oxygen-free copper lid.

where m is the mass, u is the position, and v is the velocity of the YIG sphere. The resulting oscillations are fitted to a sine curve to determine the trap frequency.

3. Eddy current estimation

Eddy current damping occurs when a magnetic object, in this case the YIG sphere, moves relative to a conductor, in this case the bobbin, and surrounding oxygen-free copper jigs. A damping force that opposes the motion of the YIG sphere arises from eddy currents, which create their own magnetic

field that opposes the original magnetic field. The magnitude of this damping force is proportional to the conductivity of the conductor, strength of the magnetic field, and velocity of the magnet. It has been the dominant loss in many magneto-mechanical systems.

A time-dependent solver in COMSOL is used to calculate the electric energy dissipated per oscillation in the YIG sphere, superconductor coil bobbin, oxygen-free copper lid, and base plate. The magnetic vector potential is calculated from

$$(j\omega\sigma - \omega^2\varepsilon)\mathbf{A} + \nabla\left(\frac{1}{\mu}\nabla \times \mathbf{A}\right) = 0, \qquad (C4)$$

where σ is the conductivity, ε is the permittivity, μ is the permeability, ω is the trap angular frequency, and $\delta = \sqrt{2/\omega\mu\sigma}$ is the skin depth. For an oxygen-free copper plate at low temperatures, the skin depth is nearly equal to the YIG diameter $\delta \sim d$. For the YIG sphere which is an insulator, the skin depth $\delta > 1$ km is sufficiently larger than the objects. In these cases, the eddy current can be calculated by volume integration of the Poynting vector as

$$P_{\text{eddy}} = \frac{1}{2}(\mathbf{J}_S \cdot \mathbf{E}*), \qquad (C5)$$

where $\mathbf{J}_S$ is the induced current and $\mathbf{E}$ is the electric field inside the object.

A time-dependent solver in COMSOL is used to calculate the electrical losses in the YIG sphere, bobbin, lid, and base plate for a single oscillation (Fig. 12). The YIG oscillation causes eddy currents in both the YIG sphere and its surroundings, which causes a displacement-dependent dissipation. Since this dissipation in the bobbin and surrounding jigs is a first-order induction effect caused by the YIG motion, while the eddy current in the YIG sphere is a second-order induction effect caused by the magnetic field change due to eddy current in the bobbin and surrounding jigs, the former is larger than the latter. In the time-dependent study, an oscillation is divided into time slots of $\delta t = 1/f/100$ s and the energy dissipation during each temporal duration is calculated. The energy dissipation per oscillation, ΔE_{eddy}, is given by the average energy loss within the oscillation. Finally, the Q factor $Q_{\text{eddy}} = 2\pi E_t/(\Delta E_{\text{eddy}})$ is estimated by comparing this to the kinetic energy $E_t = mA_z^2\omega_z^2/2$, where $m = \rho_y 4/3\pi a^3$ is the mass of the YIG sphere and A_z is the amplitude of oscillation taken from the position of the YIG.

[1] N. Kiesel, F. Blaser, U. Delić, D. Grass, R. Kaltenbaek, and M. Aspelmeyer, Proc. Natl. Acad. Sci. USA **110**, 14180 (2013).

[2] E. Turker and A. Arslan-Yildiz, ACS Biomater. Sci. Eng. **4**, 787 (2018).

[3] J. Millen, T. S. Monteiro, R. Pettit, and A. N. Vamivakas, Rep. Prog. Phys. **83**, 026401 (2020).

[4] C. Gonzalez-Ballestero, M. Aspelmeyer, L. Novotny, R. Quidant, and O. Romero-Isart, Science **374**, eabg3027 (2021).

[5] B. A. Stickler, K. Hornberger, and M. S. Kim, Nat. Rev. Phys. **3**, 589 (2021).

[6] G. Winstone, M. Bhattacharya, A. A. Geraci, T. Li, P. J. Pauzauskie, and N. Vamivakas, arXiv:2307.11858.

[7] U. Delić, M. Reisenbauer, K. Dare, D. Grass, V. Vuletić, N. Kiesel, and M. Aspelmeyer, Science **367**, 892 (2020).

[8] T. Delord, P. Huillery, L. Nicolas, and G. Hétet, Nature (London) **580**, 56 (2020).

[9] P. Huillery, T. Delord, L. Nicolas, M. Van Den Bossche, M. Perdriat, and G. Hétet, Phys. Rev. B **101**, 134415 (2020).

[10] M. Perdriat, C. Pellet-Mary, P. Huillery, L. Rondin, and G. Hétet, Micromachines **12**, 651 (2021).

[11] W.-K. Rhim, S. K. Chung, D. Barber, K. F. Man, G. Gutt, A. Rulison, and R. E. Spjut, Rev. Sci. Instrum. **64**, 2961 (1993).

[12] T. Wang, S. Lourette, S. R. OKelley, M. Kayci, Y. B. Band, D. F. Jackson Kimball, A. O. Sushkov, and D. Budker, Phys. Rev. Appl. **11**, 044041 (2019).

[13] X. Jiang, J. Rudge, and M. Hosseini, Appl. Phys. Lett. **116**, 244103 (2020).

[14] C. W. Lewandowski, T. D. Knowles, Z. B. Etienne, and B. D'Urso, Phys. Rev. Appl. **15**, 014050 (2021).

[15] Y. Leng, R. Li, X. Kong, H. Xie, D. Zheng, P. Yin, F. Xiong, T. Wu, C.-K. Duan, Y. Du, Z. Q. Yin, P. Huang, and J. Du, Phys. Rev. Appl. **15**, 024061 (2021)

[16] A. Vinante, P. Falferi, G. Gasbarri, A. Setter, C. Timberlake, and H. Ulbricht, Phys. Rev. Appl. **13**, 064027 (2020).

[17] P. Romagnoli, R. Lecamwasam, S. Tian, J. E. Downes, and J. Twamley, Appl. Phys. Lett. **122**, 094102 (2023).

[18] M. Gutierrez Latorre, A. Paradkar, D. Hambraeus, G. Higgins, and W. Wieczorek, IEEE Trans. Appl. Superconduct. **32**, 1800305 (2022).

[19] J. Hofer, R. Gross, G. Higgins, H. Huebl, O. F. Kieler, R. Kleiner, D. Koelle, P. Schmidt, J. A. Slater, M. Trupke, K. Uhl, T. Weimann, W. Wieczorek, and M. Aspelmeyer, Phys. Rev. Lett. **131**, 043603 (2023).

[20] M. Gutierrez Latorre, G. Higgins, A. Paradkar, T. Bauch, and W. Wieczorek, Phys. Rev. Appl. **19**, 054047 (2023).

[21] A. Prabhakar and D. D. Stancil, *Quantum Theory of Spin Waves* (Springer, Boston, 2009).

[22] I. S. Maksymov, J. Appl. Phys. **124**, 150901 (2018).

[23] D. Lachance-Quirion, Y. Tabuchi, A. Gloppe, K. Usami, and Y. Nakamura, Appl. Phys. Express **12**, 070101 (2019).

[24] B. Z. Rameshti, S. V. Kusminskiy, J. A. Haigh, K. Usami, D. Lachance-Quirion, Y. Nakamura, C.M. Hu, H. X. Tang, G. E. W. Bauer, and Y. M. Blanter, Phys. Rep. **979**, 1 (2022).

[25] B. Bhoi and S. K. Kim, Solid State Phys. **70**, 1 (2019).

[26] S. Haroche and J. M. Raimond, *Exploring the Quantum: Atoms, Cavities, And Photons* (Oxford University Press, Oxford, 2006).

[27] H. Huebl, C. W. Zollitsch, J. Lotze, F. Hocke, M. Greifenstein, A. Marx, R. Gross, and S. T. B. Goennenwein, Phys. Rev. Lett. **111**, 127003 (2013).

[28] Y. Tabuchi, S. Ishino, T. Ishikawa, R. Yamazaki, K. Usami, and Y. Nakamura, Phys. Rev. Lett. **113**, 083603 (2014).

[29] M. Goryachev, W. G. Farr, D. L. Creedon, Y. Fan, M. Kostylev, and M. E. Tobar, Phys. Rev. Appl. **2**, 054002 (2014).

[30] X. Zhang, C.L. Zou, L. Jiang, and H. X. Tang, Phys. Rev. Lett. **113**, 156401 (2014).

[31] L. Bai, M. Harder, P. Hyde, Z. Zhang, C. M. Hu, Y. P. Chen, and J. Q. Xiao, Phys. Rev. Lett. **118**, 217201 (2017).

[32] Y. Tabuchi, S. Ishino, A. Noguchi, T. Ishikawa, R. Yamazaki, K. Usami, and Y. Nakamura, Science **349**, 405 (2015).

[33] D. Lachance-Quirion, Y. Tabuchi, S. Ishino, A. Noguchi, T. Ishikawa, R. Yamazaki, and Y. Nakamura, Sci. Adv. **3**, e1603150 (2017).

[34] S. He, X. Xin, F. Y. Zhang, and C. Li, Phys. Rev. A **107**, 023709 (2023).

[35] R. Hisatomi, A. Osada, Y. Tabuchi, T. Ishikawa, A. Noguchi, R. Yamazaki, K. Usami, and Y. Nakamura, Phys. Rev. B **93**, 174427 (2016).

[36] J. A. Haigh, A. Nunnenkamp, A. J. Ramsay, and A. J. Ferguson, Phys. Rev. Lett. **117**, 133602 (2016).

[37] X. Zhang, N. Zhu, C. L. Zou, and H. X. Tang, Phys. Rev. Lett. **117**, 123605 (2016).

[38] A. Gloppe, M. Onga, R. Hisatomi, A. Imamoğlu, Y. Nakamura, Y. Iwasa, and K. Usami, Phys. Rev. B **105**, L121403 (2022).

[39] D. Zhang, X.-Q. Luo, Y.-P. Wang, T.-F. Li, and J. Q. You, Nat. Commun. **8**, 1368 (2017).

[40] R. C. Shen, J. Li, Z. Y. Fan, Y. P. Wang, and J. Q. You, Phys. Rev. Lett. **129**, 123601 (2022).

[41] B. Wang, X. Jia, X. H. Lu, and H. Xiong, Phys. Rev. A **105**, 053705 (2022).

[42] T. Trickle, Z. Zhang, and K. M. Zurek, Phys. Rev. Lett. **124**, 201801 (2020).

[43] N. Crescini, D. Alesini, C. Braggio, G. Carugno, D. D'Agostino, D. Di Gioacchino, P. Falferi, U. Gambardella, C. Gatti, G. Iannone, C. Ligi, A. Lombardi, A. Ortolan, R. Pengo, G. Ruoso, and L. Taffarello, Phys. Rev. Lett. **124**, 171801 (2020).

[44] X. Zhang, C. L. Zou, N. Zhu, F. Marquardt, L. Jiang, and H. X. Tang, Nat. Commun. **6**, 8914 (2015).

[45] A. Kani, B. Sarma, and J. Twamley, Phys. Rev. Lett. **128** 013602 (2022).

[46] C. Gonzalez-Ballestero, J. Gieseler, and O. Romero-Isart, Phys. Rev. Lett. **124**, 093602 (2020).

[47] C. Gonzalez-Ballestero, D. Hümmer, J. Gieseler, and O. Romero-Isart, Phys. Rev. B **101**, 125404 (2020).

[48] A. Einstein and W. De Haas, in *Proceedings Huygens Institute Royal Netherlands Academy of Arts and Sciences (KNAW)* (Amsterdam, 1915), p. 696.

[49] V. Wachter, V. A. S. V. Bittencourt, S. Xie, S. Sharma, N. Joly, P. St. J. Russell, F. Marquardt, and S. V. Kusminskiy, J. Opt. Soc. Am. B **38**, 3858 (2021).

[50] S. J. Barnett, Phys. Rev. **6**, 239 (1915).

[51] C. C. Rusconi, V. Pöchhacker, K. Kustura, J. I. Cirac, and O. Romero-Isart, Phys. Rev. Lett. **119**, 167202 (2017).

[52] C. C. Rusconi and O. Romero-Isart, Phys. Rev. B **93**, 054427 (2016).

[53] A. Kani, F. Quijandría, and J. Twamley, Phys. Rev. Lett. **129**, 257201 (2022).

[54] D. F. Jackson Kimball, A. O. Sushkov, and D. Budker, Phys. Rev. Lett. **116**, 190801 (2016).

[55] P. Fadeev, C. Timberlake, T. Wang, A. Vinante, Y. B. Band, D. Budker, A. O. Sushkov, H. Ulbricht, and D. F. J. Kimball, Quantum Sci. Technol. **6**, 024006 (2021).

[56] M. Fuwa, Phys. Rev. A **108**, 023523 (2023).

[57] M. K. Wu, J. R. Ashburn, C. J. Torng, P. H. Hor, R. L. Meng, L. Gao, Z. J. Huang, Y. Q. Wang, and C. W. Chu, Phys. Rev. Lett. **58**, 908 (1987).

[58] See Supplemental Material at http://link.aps.org/supplemental/10.1103/PhysRevA.108.063511 for a movie of the 0.3 mg mass, 0.5 mm diameter YIG levitation under an external magnetic field of 25 mT.

[59] J. W. Ekin, *Experimental Techniques for Low-Temperature Measurements* (Oxford University Press, Oxford, 2006).

[60] C. C. Rusconi, M. J. A. Schuetz, J. Gieseler, M. D. Lukin, and O. Romero-Isart, Phys. Rev. A **100**, 022343 (2019).

[61] W. Wernsdorfer and R. Sessoli, Science **284**, 133 (1999).

[62] S. R. Nair, S. Tian, G. K. Brennen, S. Bose, and J. Twamley, arXiv:2307.14553.

[63] H. Zhang and Z.-Q. Yin, Opt. Express **31**, 8139 (2023).

[64] H. Kurosawa, B. Choi, Y. Sugimoto, and M. Iwanaga, Opt. Express **25**, 4446 (2017).

[65] A. Siblini, I. Khalil, J. P. Chatelon, and J. J. Rousseau, Adv. Mater. Res. **324**, 290 (2011).

[66] Deltronic Crystal Industries product description (unpublished).

[67] S. Wittekoek, T. J. A. Popma, J. M. Robertson, and P. F. Bongers, Phys. Rev. B **12**, 2777 (1975).

[68] S. H. Wemple, S. L. Blank, J. A. Seman, and W. A. Biolsi, Phys. Rev. B **9**, 2134 (1974).

[69] S. R. Boona and J. P. Heremans, Phys. Rev. B **90**, 064421 (2014).

[70] B. T. Matthias, T. H. Geballe, and V. B. Compton, Rev. Mod. Phys. **35**, 1 (1963).

[71] C. P. Bean, Phys. Rev. Lett. **8**, 250 (1962).

[72] C. P. Bean, Rev. Mod. Phys. **36**, 31 (1964).

[73] R. Huebener, R. Kampwirth, R. Martin, T. Barbee, and R. Zubeck, IEEE Trans. Magn. **11**, 344 (1975).

[74] D. C. Larbalestier, J. Jiang, U. P. Trociewitz, F. Kametani, C. Scheuerlein, M. Dalban-Canassy, M. Matras, P. Chen, N. C. Craig, P. J. Lee, and E. E. Hellstrom, Nat. Mater. **13**, 375 (2014).